

Task-Specific Trajectory Optimisation for Twin-Robotic X-Ray Tomography

Gabriel Herl , Jochen Hiller, Mareike Thies, Jan-Nico Zaech, Mathias Unberath ,
and Andreas Maier , *Senior Member, IEEE*

Abstract—With the advent of robotic C-arm computed tomography (CT) systems in medicine and twin-robotic CT systems in industry, new possibilities for the realisation of complex trajectories for CT scans are emerging. These trajectories will increase the range of CT applications, enable optimisation of image quality for many applications and open up new possibilities to reduce scan time and radiation dose. In this work, trajectory optimisation methods for optimising both, task-based data quality and data completeness, are presented by combining two different metrics. On the one hand, task-based data quality is optimised with a proven observer model. On the other hand, a Tuy-based metric is utilised to optimise data completeness. Both metrics capture mutually exclusive properties of the trajectory which are necessary, but alone are not sufficient for trajectory optimisation. Hence, existing task-driven trajectory optimisation approaches require additional input to decide on an overall optimal trajectory, e.g. in most cases constraints on the trajectory. Advantages and disadvantages of the presented methods are investigated. It is shown that by combining both metrics, trajectory optimisation for arbitrary geometries becomes possible. In application examples it is shown that this can be used for trajectory optimisation of challenging scanning tasks involving metal parts as well as for trajectory optimisation to reduce the number of projections while ensuring task-dependently high image quality. In total, the results of this work enable new applications for X-ray CT, especially for twin-robotic CT systems which are able to benefit from a high number of degrees of freedom.

Index Terms—Computed tomography, detectability index, robotic CT, task-driven imaging, trajectory optimisation.

I. INTRODUCTION

X-RAY computed tomography (CT) allows a high-precision, three-dimensional digitisation of inner and

Manuscript received November 30, 2020; revised March 24, 2021 and June 17, 2021; accepted August 2, 2021. Date of publication August 11, 2021; date of current version September 1, 2021. This work was supported in part by the project “MultiPosCT” which was funded by the “Bayerisches Staatsministerium für Wissenschaft und Kunst” (as part of the “Strukturimpuls Forschungseinstieg 2017”). The work of Gabriel Herl was supported by BayWISS Consortium “Digitization”. The associate editor coordinating the review of this manuscript and approving it for publication was Dr. Webster Stayman. (*Corresponding author: Gabriel Herl.*)

Gabriel Herl is with the Deggendorf Institute of Technology, 94469 Deggendorf, Germany, and with Fraunhofer EZRT, 90768 Fürth, Germany (e-mail: gabriel.herl@th-deg.de).

Jochen Hiller is with the Deggendorf Institute of Technology, 94469 Deggendorf, Germany (e-mail: jochen.hiller@th-deg.de).

Mareike Thies and Andreas Maier are with the Pattern Recognition Lab, University of Erlangen-Nuremberg, 91054 Erlangen, Germany (e-mail: thies.mareike@fau.de; andreas.maier@fau.de).

Jan-Nico Zaech is with the Computer Vision Lab, ETH Zürich, 8092 Zurich, Switzerland (e-mail: jan-nico.zaech@vision.ee.ethz.ch).

Mathias Unberath is with the Laboratory for Computational Sensing and Robotics, Johns Hopkins University, Baltimore, MD 21218 USA (e-mail: unberath@jhu.edu).

Digital Object Identifier 10.1109/TCI.2021.3102824

2333-9403 © 2021 IEEE. Personal use is permitted, but republication/redistribution requires IEEE permission.
See <https://www.ieee.org/publications/rights/index.html> for more information.

outer structures of living organisms as well as industrial objects. CT therefore has enormous potential in both, medicine [1] and industry [2]. In order to generate a three-dimensional, digital image of the region of interest, two-dimensional projections must be generated from different vantage angles. In conventional CT systems, CT scans are typically carried out using circular trajectories by rotating an industrial object or by moving the X-ray source and the X-ray detector in a circle around an examination region. A circular scanning trajectory is sufficient for many applications, but only allows limited optimisation for application-specific adaptations for complex inspection tasks, dose reduction or artefact avoidance.

In medicine as well as in industry, there are two main reasons for non-standard trajectories. Firstly, a circular trajectory might not be possible due to lack of space. This is relevant when scanning particularly large objects, e.g. in the automotive or aerospace industry, but also in medicine, when space in the operating room is limited due to a variety of necessary tools and when patients are obese. Secondly, metal artefacts pose a major challenge for CT imaging. Whenever X-rays penetrate metal, physical effects can lead to artefacts in the reconstruction and reduce the image quality. Both in medicine [3] and industry [4], [5], these metal artefacts can be avoided or reduced by adapting the CT trajectory in such a way that as few of the relevant rays as possible have to penetrate metal. A relevant example from industry is the investigation of a built-in rear light in an automobile. With ordinary acceleration energies below several mega electron volts, the X-ray radiation cannot sufficiently penetrate the entire vehicle. Hence, a scan using a circular trajectory would not be able to generate enough information for reconstruction due to total absorption. However, by utilising a complex scan trajectory, for example by placing the X-ray source partially in the trunk, a scan with sufficient image quality can be made possible.

In order to create a more flexible CT system that is capable of performing such complex trajectories, the X-ray source and the X-ray detector can be mounted on robots. In medicine, so-called C-arm CT systems are already in use, in which the source and the detector are attached to a C-arm that is moved by a single robot. In the past decades, these C-arm CT systems have already led to many new medical applications, e.g. in angiography [6], in radiology [7] or for spine interventions [8]. In recent years, research has been carried out on twin-robotic CT systems for medical [9] as well as industrial applications [10]. In twin-robotic CT systems the source and the detector can



Fig. 1. A twin-robotic CT system at the deggendorf institute of technology.

each be moved separately by a robot and, hence, the flexibility of the system increases enormously. These twin-robotic CT systems are far from being as mature as the C-arm systems, but they give rise to many new applications. A recently established industrial twin-robotic CT system at the Deggendorf Institute of Technology is shown in Fig. 1.

The use of robots creates new degrees of freedom that enable application specific scan trajectories. However, the question arises how this scan trajectory should be selected for specific applications in order to achieve optimal digitisation results. Especially in the medical field, preliminary work for trajectory optimisation of C-arm CT systems is already in place. One of the most promising approaches is that of Stayman *et al.* [11] where a detectability index based on a non-prewhitening observer model is optimised for individually customizable task functions based on prior knowledge, e.g. the anatomy of a specific patient including the position of implants. Zaech *et al.* [3] built on this approach of Stayman *et al.* by utilising machine learning in order to enable a live optimisation of the trajectory without prior knowledge. Other examples for trajectory optimisation are Hatamikia *et al.* [12] who optimised trajectories by looking for optimally complementary short scans and Zheng *et al.* [13] who looked for X-rays tangential to edges of a previously known object to maximise the edge information. In the industrial environment, there has been less research about the optimisation of robotic trajectories. Fischer *et al.* [14] implemented the approach of Stayman *et al.* for industrial use cases using CAD data. Wu *et al.* [15] optimised trajectories by minimising the difference of polychromatic and monochromatic X-ray simulations in order to avoid metal artefacts. Additionally, in preliminary work, the authors presented an approach for trajectory optimisation using a measure based on the well known Tuy conditions [5] in order to ensure sufficient vantage angles while also avoiding metal artefacts.

The currently existing methods either analyse directly the reconstructions from simulations, which is computationally costly, or optimise a special quality measure. However, both in medicine and in industry, the authors are not currently aware of any trajectory optimisation method that optimises both, data quality and data completeness jointly. Therefore, all known methods need additional input for the choice of an overall

optimal trajectory. For example, the mentioned approach of Stayman *et al.* [11] optimises a detectability index whereby the data quality of the projections in the trajectory is optimised. However, the detectability index does not consider the data completeness and, hence, does not consider to which extent an individual projection in combination with other projections actually provides added value in the form of new information. In order to ensure that projections from sufficient directions are actually generated, artificial constraints were indirectly introduced. For example in [11] Stayman *et al.* demand that a trajectory is constructed from certain basic functions which assign a tilt angle to each rotation angle while the source-focus-distance and detector-focus-distance remain constant. This parameterisation of trajectories strongly limits the space of possible trajectories and, hence, for many use cases prevents optimal trajectories. Therefore, the full potential of robotic CT systems cannot yet be fully exploited.

In this paper, we combine the work of Stayman *et al.* [11] with preliminary work of the authors [5] in order to optimise both, data quality and data completeness. Using this approach, application-specific scan trajectories can be found based only on mathematical conditions without limiting restrictions to the parametrisation of the trajectory or additional input. The content of this work will be applicable both for medical C-arm CT systems as well as industrial robot based CT systems.

The work is organised as follows. In Section II four different approaches for optimising CT trajectories are presented. In Section III experiments based on simulation and measurement data are presented and discussed. Section IV concludes this work.

II. METHODS

A. Basic Approach of Trajectory Optimisation

In order to optimise a trajectory for a given use case, all of the presented approaches in this work will include three important parts based on three key questions.

- 1) **What does optimal mean?** A quality function is needed that quantifies the extent to which a trajectory meets the requirements of the application. This quality function can differ from case to case depending on the requirements. In this work, we will use the detectability index of the non-prewhitening observer model following Stayman *et al.* [11] as well as a Tuy-based measure of preliminary works of the authors [5] which will be discussed in detail later.
- 2) **What exactly is a trajectory?** In order to optimise a trajectory, we first have to define what we actually mean by trajectory. In the sense of this work, a trajectory is described by a set of acquisition geometries $G := \{g_1, g_2, \dots, g_n\}$ with $n \in \mathbb{N}$ as the number of projections where every $g_i, i \leq n$, contains all necessary geometrical information for one X-ray projection. The implementation of these acquisition geometries g_i can vary and is part of this work. Furthermore, let $p \in \mathbb{R}^{m \times m}$ be a single projection consisting of the measurements of the detector pixel values with $m \in \mathbb{N}$ the number of detector pixels in horizontal and vertical direction. In order to create realistic

projections, we simulate the X-ray pROCESS according to the given acquisition geometries. Hence, for the approaches of this work, prior knowledge is needed, e.g. in the form of a CAD model of the object to be scanned. Let $P : G \rightarrow \mathbb{R}^{m \times m}$ denote a function for the simulation of a projection corresponding to a given acquisition geometry.

- 3) **How can a trajectory be optimised?** Finding a trajectory that is optimal according to a chosen parametrisation and a chosen quality function demands an appropriate algorithmic approach. Trajectory optimisation is an enormously complex, highly non-convex problem. Hence, finding a global optimum is costly and challenging. To address this challenge, sophisticated evolutionary algorithms like the covariance matrix adaptation evolution strategy (CMA-ES) [16] can be utilised. However, finding a global optimum is not the focus of this work. Instead, in this work a greedy approach is used that does not guarantee an optimal solution, but ensures a feasible runtime. In this greedy approach, the best acquisition geometry from a given basic set of acquisition geometries is iteratively selected and added to the optimised trajectory. Therefore, firstly, a basic set $G_{all} := \{g_1, g_2, \dots, g_{\tilde{n}}\}$ has to be constructed which contains all admissible options of acquisition geometries with \tilde{n} the number of projections in the basic set. The specific implementation of this basic set and also of the greedy approach depends on the use case and will be elaborated in greater detail in the following sections.

B. Trajectory Optimisation Based on the Detectability Index of the Non-Prewhitening Observer Model

The modulation transfer function MTF and the noise power spectrum NPS for the penalized likelihood reconstruction method can be approximated as in [17]:

$$MTF_j \approx \frac{\mathcal{F}\{\mathbf{A}^\top \mathbf{D} \mathbf{A} e_j\}}{\mathcal{F}\{\mathbf{A}^\top \mathbf{D} \mathbf{A} e_j + \beta \mathbf{R} e_j\}}, \quad (1)$$

$$NPS_j \approx \frac{\mathcal{F}\{\mathbf{A}^\top \mathbf{D} \mathbf{A} e_j\}}{|\mathcal{F}\{\mathbf{A}^\top \mathbf{D} \mathbf{A} e_j + \beta \mathbf{R} e_j\}|^2}, \quad (2)$$

where \mathbf{A} is the system matrix, modelling the contribution of every voxel to every projection measurement, \mathbf{D} denotes the diagonal matrix of projection measurements, e_j is a unity vector with one at only one entry that specifies the location of interest. Furthermore, \mathbf{R} is a quadratic penalty of the penalized likelihood reconstruction method with a weight β .

Using these estimations, Stayman *et al.* derived an approximation for the detectability index of the non-prewhitening matched filter observer model. This approximation allows conclusions about the local spatial resolution and noise properties and, hence, can be used as a quality function. Based on a task function T which specifies the spatial frequencies of interest, the detectability index $d^{\prime 2}$ of the chosen non-prewhitening model can be written as

$$d_x^{\prime 2}(G, T) = \frac{\left(\int [MTF_x(G) \cdot T]^2 df\right)^2}{\left(\int NPS_x(G) \cdot [MTF_x(G) \cdot T]^2 df\right)} \quad (3)$$

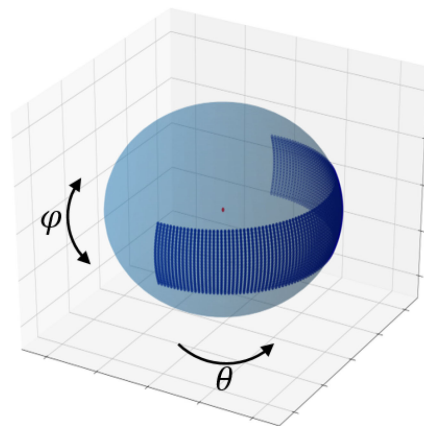


Fig. 2. A visualisation of the source positions of an exemplary trajectory basic set based on the parametrisation of Algorithm 1: The dark blue dots represent exemplary source positions. Every source position is on a sphere and determined by a rotation angle θ and a tilt angle φ . In this example, a trajectory basic set is given by restrictions to the possible angles: $G := \{(\theta, \varphi) : 0^\circ \leq \theta \leq 180^\circ \wedge -18^\circ \leq \varphi \leq 18^\circ\}$.

where the subscript x indicates the spatial position of interest in the reconstructed volume.

For the parametrisation of the trajectory, i.e. the set of acquisition geometries G , Stayman *et al.* mostly considered orbits that sample a circular band around the region of interest by defining a function that maps from a rotation angle θ to a tilt angle φ on a sphere as visualised in Fig. 2. The other geometrical parameters like source-focus distance, detector-focus distance and translations remain fixed. An acquisition geometry can then be specified by a pair of rotation angle and tilt angle: $g := (\theta, \varphi)$.

As the most flexible variant of this parameterisation approach, Zaech *et al.* optimised trajectories in [3] by looking for the optimal tilt angle φ for each chosen rotation angle θ separately. Let α be the angle which determines the sampling angle on a sphere and β be the angle of maximal rotation. Furthermore, let $\Theta := \{\theta_i : \theta_i = i\alpha, 0 \leq \theta_i \leq \beta, i \in \mathbb{N}_0\}$ be the set of all chosen rotation angles. Furthermore, let $\Phi := \{\varphi_i : \varphi_i = i\alpha, -\gamma \leq \varphi_i \leq \gamma, i \in \mathbb{N}_0\}$ be the set of all admissible tilt angles for the optimisation pROCESS with γ defining the maximal tilt of the vantage angles in relation to the horizontal. In the sense of Zaech *et al.*, a set of acquisition geometries can be defined as $G := \{(\theta, \varphi) : \theta \in \Theta \wedge \varphi \in \Phi\}$.

Using the parametrisation of Zaech *et al.* and the detectability index following Stayman *et al.* as the quality function, the problem of finding an optimised trajectory can be implemented by finding the tilt angle that maximises $d^{\prime 2}$ for each rotation angle. Following Zaech *et al.* [3], $d^{\prime 2}$ is calculated for every possible projection separately in order to evaluate the quality of every projection in a computationally efficient way. A short pseudo implementation of an optimisation workflow is presented in Algorithm 1.

By optimising the tilt angle for every rotation angle, the trajectory automatically includes vantage angles from every chosen rotation angle. Depending on the maximum allowed tilt angle, the maximum deviation from a circular trajectory is limited. Hence, the resulting trajectory usually provides

Algorithm 1: $Opt_{Detectability}$.

Input : Task function T
 Locality of interest x
 Set of rotation angles Θ
 Set of feasible tilt angles Φ

Output: An optimised trajectory G

Set $G_0 := \{\}$ and $i := 0$;
for $\theta_i \in \Theta$ **do**
 Calculate $\varphi^* := \arg \max_{\varphi \in \Phi} d_x'^2(\{(\theta_i, \varphi)\}, T)$;
 Set $G_{i+1} := G_i \cup \{(\theta_i, \varphi^*)\}$;
 Update $i \leftarrow i + 1$;
Return G_{i+1} as G .

Algorithm 2: Opt_{Max} .

Input : Task function T
 Locality of interest x
 Basic trajectory G_{all}
 Number $n \in \mathbb{N}$ of wanted projections

Output: An optimised trajectory $G \subset G_{all}$

Set $G_0 := \{\}$ and $i := 0$;
while $i < n$ **do**
 Calculate $g^* := \arg \max_{g \in G_{all}} d_x'^2(\{g\}, T)$;
 Set $G_{i+1} := G_i \cup \{g^*\}$;
 Update $i \leftarrow i + 1$;
Return G_{i+1} as G .

information from sufficient directions. However, the orientation of this circle-like trajectory is dependent on user input and therefore needs prior knowledge about the scan scenario. Furthermore, this kind of parametrisation limits the degrees of freedom of the trajectory strongly and excludes a remarkable number of trajectories. In particular, in this type of approach, the number of chosen projections has to be equal to the number of rotational steps. This means that the number of projections can only be reduced by increasing the rotational step size. Hence, a reduction of the number of projections automatically decreases the angular resolution. Furthermore, as there has to be a projection from any angle of rotation, the focus of the trajectory on the scan task is restricted.

In order to allow all kinds of possible trajectories, we suggest the following parametrisation for trajectory acquisition geometries. Let $G := \{g_1, g_2, \dots, g_n\}$ be the set of acquisition geometries g_i of n projections with $g_i := \{l_{source,i}, l_{detector,i}, o_{source,i}, o_{detector,i}\}$ consisting of the location of the source $l_{source,i} \in \mathbb{R}^3$ and the detector $l_{detector,i} \in \mathbb{R}^3$ as well as the orientation of the source $o_{source,i} \in \mathbb{R}^3$ and the detector $o_{detector,i} \in \mathbb{R}^3$ for projection i .

With a sufficiently big basic trajectory G_{all} consisting of all admissible possible acquisition geometries, this kind of parametrisation allows completely free optimisation of arbitrary trajectories. Iteratively choosing the acquisition geometry that optimises the detectability index, the new problem Opt_{max} can be formalised as written in Algorithm 2.

The detectability index d'^2 estimates and optimises the data quality of the projections in the trajectory. However, the detectability index does not estimate the data completeness, i.e. the extent to which a projection in combination with the other projections actually provides additional value in the form of new information. Hence, using only the detectability index, projections from sufficient directions cannot be ensured.

C. Trajectory Optimisation Based on a Tuy-Based Measure

In order to allow more flexible trajectories without further input or limitations, it is necessary to add an additional measure for the data completeness to the quality function that ensures that projections from different vantage angles are added to the trajectory. The well-known Tuy conditions determine whether a

volume can be reconstructed mathematically correct [18]. The main condition states that every possible plane through any voxel of the volume has to intersect with the trajectory. However, the Tuy conditions only state whether a given scenario allows ideal reconstruction or not. Furthermore, the Tuy conditions are completely object independent and do not consider the attenuation of the object under examination. Therefore, the Tuy conditions alone cannot be used for trajectory optimisation. In preliminary work [5], the authors have introduced a local, object dependent measure based on the Tuy conditions that can be used for trajectory optimisation. Likewise, in [19], Gang *et al.*, introduced a similar approach. The basic idea of this measure is to indicate how close a given trajectory is to the fulfilment of the Tuy condition. To obtain a local, object-dependent measure, only those parts of the trajectory are considered for which the attenuation in the projections are not too high at the region of interest.

In order to present this object-dependent measure M_{Tuy} in detail, some definitions are needed. For each image geometry g_i and each spatial position x , an X-ray beam is denoted by the normalised direction vector $d_{i,x}$ given by $d_{i,x} := \frac{l_{source,i} - x}{\|l_{source,i} - x\|_2}$. Furthermore, let

- $p_{i,x} \in P(g_i)$ be the remaining intensity of this beam measured at the detector, i.e. the corresponding pixel value of projection i , after penetration of the object under examination,
- $t \in \mathbb{R}_0^+$ be a threshold for the minimally admissible remaining X-ray intensity,
- $D_{x,G,t} := \{d := \frac{l_{source,i} - x}{\|l_{source,i} - x\|_2} \mid g_i \in G \wedge p_{i,x} \geq t\}$ be the set of normed vectors d denoting X-ray beams through the voxel of interest that are not attenuated too much corresponding to the threshold t .

For a trajectory G , the spatial position of interest x and a given plane through position x represented by its normal vector u , the angular distance $\psi_G(x, u, t)$ to the closest admissible point on the trajectory can be calculated with

$$\psi_G(x, u, t) := \arg \min_{d \in D_{x,G,t}} |d^\top u|. \quad (4)$$

By discretely sampling the unit sphere \mathbb{S} and averaging the distances $\psi_G(x, u, t)$ for every plane with normal vector $u \in \mathbb{S}$

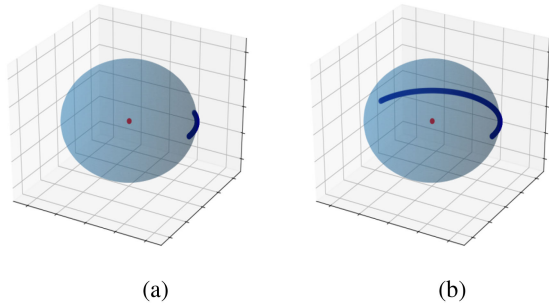


Fig. 3. Limited angle trajectories: Trajectory (a) has a scan angle of 45° and a relatively high normed measure $M_{Tuy} \approx 0.61$ for the red visualised centre point. Trajectory (b) has a scan angle of 170° and a significantly lower normed measure $M_{Tuy} \approx 0.04$ for the red visualised centre point.

Algorithm 3: Opt_{Tuy} .

Input : Locality of interest x
 Basic trajectory G_{all}
 Number $n \in \mathbb{N}$ of wanted projections

Output: An optimised trajectory $G \subset G_{all}$

Set $G_0 := \{\}$ and $i := 0$;

while $i \leq n$ **do**

Calculate

$g^* := \arg \min_{g \in G_{all}} M_{Tuy}(x, G_i \cup \{g\}, t)$;

Set $G_{i+1} := G_i \cup \{g^*\}$;

Update $i \leftarrow i + 1$;

Return G_{i+1} as G .

through position x , we generate a local, Tuy-based measure:

$$M_{Tuy}(x, G, t) := \frac{1}{|\mathbb{S}|} \sum_{u \in \mathbb{S}} \psi_G(x, u, t) \quad (5)$$

Assuming the unit sphere is sampled sufficiently, if this measure is 0, the main condition of the Tuy conditions is fulfilled and a complete reconstruction is possible. If this measure is not 0, but close to 0, information from some directions is missing. However, depending on the application, a sufficiently good reconstruction may still be possible. If this measure is not close to 0, many necessary viewing angles are missing and a sufficient reconstruction of the region of interest is unlikely. Examples of two trajectories and their Tuy-based measure M_{Tuy} are presented in Fig. 3.

With the presented parameterisation and the help of the Tuy-based measure $M_{Tuy}(x, G, t)$, the optimisation problem Opt_{Tuy} can be approached greedily by iteratively adding the next best acquisition geometry g to the current trajectory as presented in Algorithm 3.

In order to achieve an optimisation approach that both optimises data quality and data completeness, the approaches $Opt_{Detectability}$ and Opt_{Tuy} can be combined. By forming the quotient of the detectability index d'^2 and the proposed Tuy-based measure M_{Tuy} , a new measure $M_{combined}$ can be written as

$$M_{combined}(x, G, t, T) := \frac{M_{Tuy}(x, G, t)}{d'_{Task}{}^\alpha(G, T)}, \quad (6)$$

Algorithm 4: $Opt_{Combined}$

Input : Task function T
 Locality of interest x
 Basic trajectory G_{all}
 Number $n \in \mathbb{N}$ of wanted projections

Output: An optimised trajectory $G \subset G_{all}$

Set $G_0 := \{\}$ and $i := 0$;

while $i \leq n$ **do**

Calculate $g^* := \arg \min_{g \in G_{all}} \frac{M_{Tuy}(x, G_i \cup \{g\}, t)}{d'_x{}^2(\{g\}, T)}$;

Set $G_{i+1} := G_i \cup \{g^*\}$;

Update $i \leftarrow i + 1$;

Return G_{i+1} as G .

where $\alpha \in \mathbb{R}_0^+$ denotes a weighting factor to control the influence of the two different measures.

In order to jointly optimise both, data quality and completeness, a greedy approach can be utilised by iteratively adding the acquisition geometry that optimises data quality for the complete trajectory while only contributing high quality information. This acquisition geometry g can be determined by the quotient of the completeness measure $M_{Tuy}(x, G_i \cup \{g\}, t)$ of the resulting complete trajectory and the detectability index $d'_x{}^2(\{g\}, T)$ of the examined single acquisition geometry. An optimisation approach for this combined approach is shown in Algorithm 4.

The four presented algorithms are briefly summarised in Table I.

III. EXPERIMENTS, RESULTS AND DISCUSSION

For proof and visualisation of the presented optimisation approaches, experiments on simulations and measurement data are conducted. The goal of these experiments is to demonstrate the advantages of the presented approaches, especially of Opt_{max} and $Opt_{Combined}$. Experiments for the optimisation method Opt_{Tuy} from Algorithm 3 with only the Tuy-based measure, but without the detectability index d'^2 , have already been presented in [5] and, hence, are not part of this work. In contrast to $Opt_{Detectability}$, Opt_{Max} and $Opt_{Combined}$ are able to optimise trajectories that are not restricted to spherical trajectories. However, to ensure comparability of the presented methods, the parameterisation of basic trajectories in this work is always based on a sphere. More complex basic trajectories are again shown in [5].

In the first experiment, a trajectory optimisation task with two different basic sets of acquisition geometries is presented in order to show the differences in the dependency of the algorithms relating to the choice of the basic set. In the second experiment, another task dependent example of a trajectory optimisation use case with the goal of finding a good trajectory with a small amount of projections is shown. The different approaches are tested and the differences are evaluated. The last example proves that our method is applicable to real data by applying $Opt_{Combined}$ from Algorithm 4.

TABLE I
OVERVIEW OF THE PRESENTED METHODS FOR TRAJECTORY OPTIMISATION

Method	Parametrisation of trajectories	Quality function	Description
$Opt_{Detectability}$	One tilt angle per rotation angle located on a sphere with fixed focus-detector distance	Detectability index d'^2	Task and object dependent trajectory optimisation with strong limitations to the set of possible trajectories due to the parametrisation.
Opt_{max}	Location and orientation of source and detector	Detectability index d'^2	Task and object dependent trajectory optimisation with no limitations to the trajectories, but no consideration of sufficient vantage angles
Opt_{Tuy}	Location and orientation of source and detector	Tuy-based measure M_{Tuy}	Object dependent trajectory optimisation without limitations to the trajectories while ensuring sufficient vantage angles, but no task dependency
$Opt_{Combined}$	Location and orientation of source and detector	Tuy-based measure M_{Tuy} , detectability index d'^2	Task and object dependent trajectory optimisation without limitations to the trajectories while ensuring sufficient vantage angles

For the reconstruction, an adapted algebraic reconstruction method based on preliminary work of the authors [4] was used in order to reduce metal artefacts by downweighting strongly attenuated X-ray beams.

For the approximation of the detectability index, the MTF and NPS were approximated following the approach of Stayman. *et al.* [17]. For the evaluation of $\mathbf{A}^T \mathbf{D} \mathbf{A} e_j$, the core part of these approximations, a ray based implementation has been utilised.

This estimator of the detectability index is based on approximations for the MTF and NPS of the penalized-likelihood reconstruction. Hence, strictly speaking, the estimator only applies to volumes reconstructed by penalised-likelihood reconstruction. However, we rely on the assumption that a trajectory that enables optimal reconstruction for penalised-likelihood reconstruction, according to this estimator, automatically generates sufficient data for a high quality reconstruction with other reconstruction methods, too.

In every experiment, a single voxel x , roughly centred at the expected location of the task, has been chosen as locality of interest for the calculation of the presented figures of merit. The parameter α for $Opt_{Combined}$ has been set to 1 and not changed in this work.

The simulations are performed using polychromatic spectrum and simulative noise, but no scatter simulation. The scan parameters of the simulations are 225 kV, no prefilter, a pixel size of $700 \mu\text{m}$, a detector pixel matrix of 256×256 and a magnification of factor 3. The voxel size of the reconstruction is $234 \mu\text{m}$.

A. Simulation Experiment 1

For the first experiment, the goal was to optimally visualise three cylindrical holes in a carbon test specimen of 3 cm height as shown in Fig. 4 a. Therefore, a simple task function consisting of a cylinder parallel to the X-axis as shown in Fig. 4 b was chosen. This task function ensures that the detectability index increases if central, cylindrical structures with alignment to the X-axis are well detected.

To emulate a difficult scanning task, the carbon test specimen has been placed between two iron plates of 1 cm width. Projections of this setup are shown in Fig. 5.

In experiment 1a, acquisition geometries on a sphere have been used as a basic trajectory. Using an angular step size of 2° , the basic set contains 100 rotational view angles equally

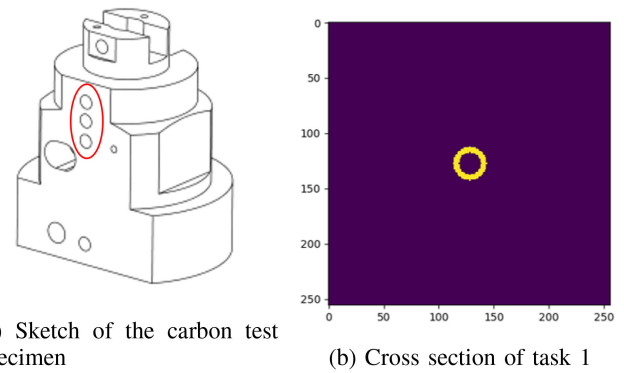


Fig. 4. Setting of experiment 1: In (a) a sketch of the carbon test specimen used in experiment 1 is shown. The red circle highlights three holes indicating the task for the optimisation process. Section (b) shows a section of the cylindrical task function in the y - z -plane.

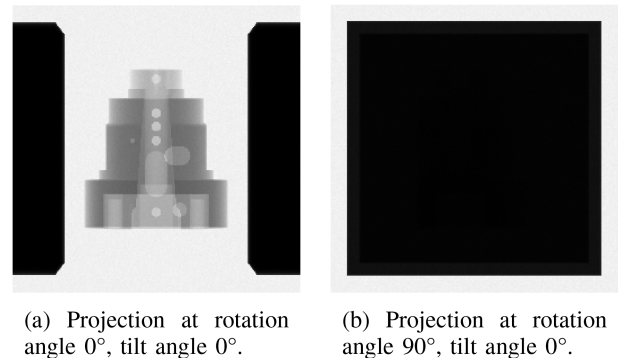


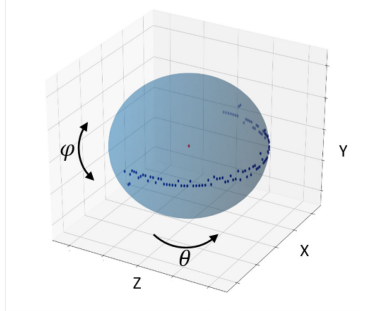
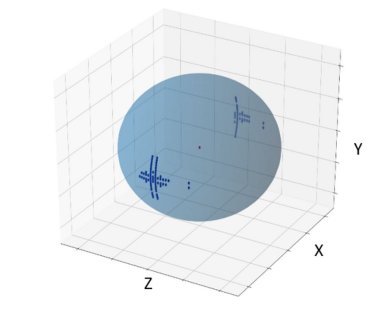
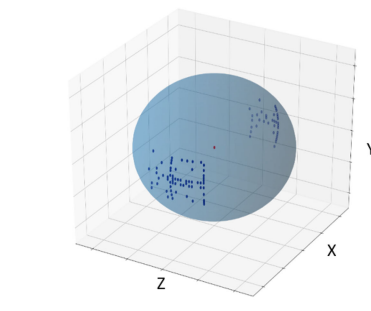
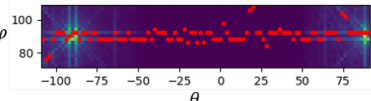
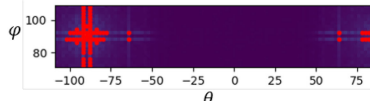
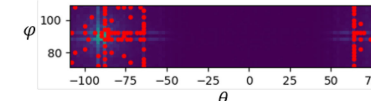
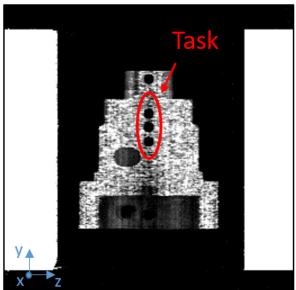
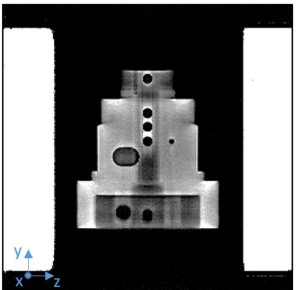
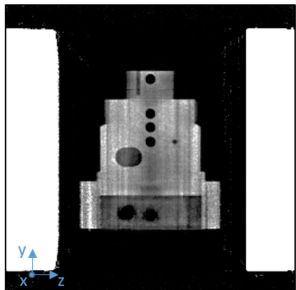
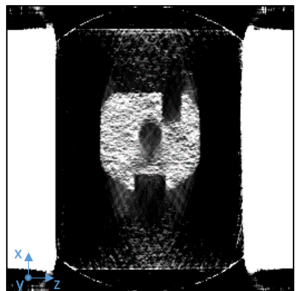
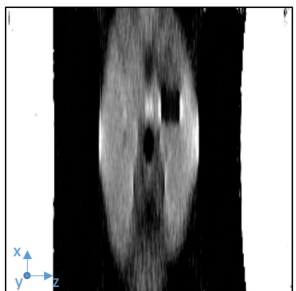
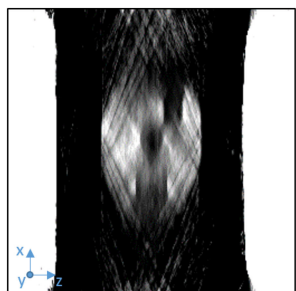
Fig. 5. Two projections of the carbon test specimen between two iron plates in experiment 1 scanned at different angles. The projection in (b) is almost completely black due to the metal plates that attenuate most of the photons.

distributed on a circular arc of 200° and 19 possible tilt view angles between -18° and 18° angle from the horizontal in order to allow projections in a relatively narrow circular band with 1900 projections, visualised in Fig. 6.

Trajectories have been optimised with the algorithms $Opt_{Detectability}$, Opt_{Max} and $Opt_{Combined}$ with the goal of $n := 100$ optimal projections. The reconstruction results are visualised in Table II. For quantitative comparison, the contrast-noise-ratio (CNR) as well as the total variation (TV) have been calculated on a small region around the task. Furthermore, the

TABLE II

RESULTS OF EXPERIMENT 1A: EACH COLUMN SHOWS THE RESULTS OF ONE OF THE OPTIMISATION ALGORITHMS. THE FIRST ROW SHOWS A 3D VISUALISATION OF THE TRAJECTORIES. EACH DARK BLUE DOT REPRESENTS THE SOURCE POSITION OF ONE ACQUISITION GEOMETRY. THE SECOND ROW SHOWS A PLANAR VISUALISATION OF THE TRAJECTORIES REPRESENTED BY RED DOTS ON A GRID WITH THE VERTICAL AXIS SHOWING THE TILT ANGLE AND THE HORIZONTAL AXIS SHOWING THE ROTATION ANGLE. THE GRID PIXELS VISUALISE THE NORMED VALUE OF THE DETECTABILITY INDEX OF THE CORRESPONDING PROJECTION WITH LIGHT COLOURS REPRESENTING A HIGH DETECTABILITY INDEX. THE THIRD AND THE FOURTH ROW SHOW SECTIONS OF THE RESULTING RECONSTRUCTIONS. THE THIRD ROW, I.E. THE Y-Z-PLANE, REPRESENTING THE SECTION THAT SHOULD HAVE OPTIMISED IMAGE QUALITY DUE TO THE CHOICE OF THE TASK FUNCTION WHICH IS VISUALISED IN (G)

<i>OptDetectability</i>	<i>OptMax</i>	<i>OptCombined</i>
 <p>(a) 3D visualisation of the trajectory</p>	 <p>(b) 3D visualisation of the trajectory</p>	 <p>(c) 3D visualisation of the trajectory</p>
 <p>(d) Planar visualisation of the trajectory</p>	 <p>(e) Planar visualisation of the trajectory</p>	 <p>(f) Planar visualisation of the trajectory</p>
 <p>(g) Reconstruction, y-z-plane</p>	 <p>(h) Reconstruction, y-z-plane</p>	 <p>(i) Reconstruction, y-z-plane</p>
 <p>(j) Reconstruction, x-z-plane</p>	 <p>(k) Reconstruction, x-z-plane</p>	 <p>(l) Reconstruction, x-z-plane</p>

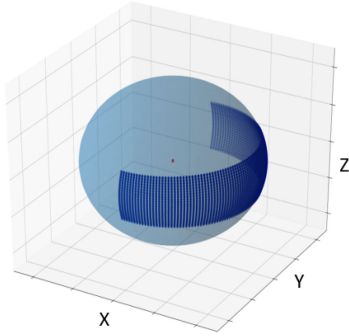


Fig. 6. Source positions of the basic trajectory of experiment 1a, a relatively narrow circular band with 2100 projections in total. Every dark blue dot represents one source position.

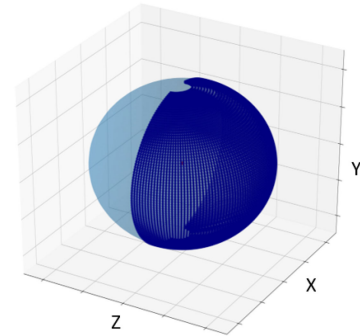


Fig. 7. Source positions of the basic trajectory of experiment 1b, a wide circular band almost equal to a half sphere. Every dark blue dot represents one source position.

TABLE III

IMAGE METRICS OF EXPERIMENT 1A: EVALUATION OF THE PRESENTED MEASURE M_{Tuy} AS WELL AS THE CNR AND THE TV IMAGE METRIC ON SMALL, TASK-CENTRED REGIONS OF THE VOLUMES OF EXPERIMENT 1A AS WELL AS THE CORRESPONDING

Method	CNR	TV	M_{Tuy}
$Opt_{Detectability}$	39.0	0.122	0.063
Opt_{Max}	32.3	0.058	0.087
$Opt_{Combined}$	79.6	0.044	0.063

presented measure M_{Tuy} has been calculated for all trajectories to compare their data completeness. The quantitative results are shown in Table III.

In $Opt_{Detectability}$ an acquisition geometry must be selected at each angle of rotation. Hence, a great percentage of the chosen projections does not focus on the task (as can be seen in row 2 of Table II) and, furthermore, does not avoid views through the metal plates which absorb almost all passing photons. Therefore, the reconstruction results are noisy and contain artefacts. The task, the three central holes in X-direction, cannot be seen properly.

In Opt_{Max} and $Opt_{Combined}$ acquisition geometries at each angle of rotation are not needed. Hence, both resulting trajectories avoid views through the metal plates. The trajectory of Opt_{Max} completely focuses on the chosen task and, therefore, only chooses projections roughly perpendicular to the y-z-plane. The trajectory of $Opt_{Combined}$ also focuses on the chosen task, but also contains some views from other directions. This focus on the chosen task results in a clear visibility of the task, the three central holes, in the reconstructions of both, Opt_{Max} and $Opt_{Combined}$. However, this focus on the chosen task leads to a worse reconstruction for other parts and directions in the reconstruction, e.g. the x-z-plane.

Both, CNR and TV, indicate that the image quality in the region of the task is best for $Opt_{Combined}$. Due to less noise and sharp edges, Opt_{Max} has a smaller TV than $Opt_{Detectability}$. However, due to the focus on the task, the grey value distribution in other directions is not homogeneous and, hence, Opt_{Max} has a worse CNR than $Opt_{Detectability}$. M_{Tuy} is equal for $Opt_{Detectability}$ and $Opt_{Combined}$ as the data completeness of both methods is close to optimal in this restricted use case. M_{Tuy}

is worse for Opt_{Max} as it does not consider data completeness in any way.

In order to increase the image quality of the results, we perform experiment 1b by expanding the set of possible acquisition geometries to a wider circular band with 86 possible tilt angles between -85° and 85° from the horizontal and, again, 100 rotational view angles equally distributed on a circular arc of 200° . The set of this expanded possible acquisition geometries with 8600 total positions is visualised in Fig. 7.

Again, trajectories have been optimised with the algorithms $Opt_{Detectability}$, Opt_{Max} and $Opt_{Combined}$ with the goal of $n := 100$ optimal projections. The results are visualised in Table IV. Furthermore, quantitative image metrics are shown in Table V.

In $Opt_{Detectability}$, with a greater possible tilt angle, views through the metal plates are avoided. Therefore, the reconstruction results are much better and the task, the three central holes, can be seen clearly. The trajectory of Opt_{Max} did not change much in comparison to the trajectory of experiment 1a, as the views with the best detectability have already been possible with the first basic trajectory. Hence, the results do not improve much. This means that the task, the three central holes, is still clearly visible, but the other directions, e.g. the x-z-plane are still of poor image quality. Without any prior knowledge, the trajectory of $Opt_{Combined}$ strongly resembles a circular trajectory that completely avoids the metal plates. This leads to the best image quality according to the complete object and the task which is clearly visible.

In experiment 1b, $Opt_{Combined}$ clearly is better than $Opt_{Detectability}$ visually as well as in all measured quantitative metrics. Especially the high CNR indicates that the image quality in the region of the task is best for $Opt_{Combined}$. Due to little noise and sharp edges, Opt_{Max} has the smallest TV. However, due to the focus on the task, the grey value distribution in other directions is not homogeneous and, hence, Opt_{Max} has the worst CNR. M_{Tuy} is almost zero for $Opt_{Combined}$, indicating a Tuy-complete trajectory. M_{Tuy} is worse for $Opt_{Detectability}$ and even worse for Opt_{Max} , demonstrating a decreasing consideration of data completeness.

To summarise experiment 1, $Opt_{Detectability}$ mostly visualises the task. However, the image quality, according to the

TABLE IV

RESULTS OF EXPERIMENT 1B: EACH COLUMN SHOWS THE RESULTS OF ONE OF THE OPTIMISATION ALGORITHMS. THE FIRST ROW SHOWS A 3D VISUALISATION OF THE TRAJECTORIES. EACH DARK BLUE DOT REPRESENTS THE SOURCE POSITION OF ONE ACQUISITION GEOMETRY. THE SECOND ROW SHOWS A PLANAR VISUALISATION OF THE TRAJECTORIES REPRESENTED BY RED DOTS ON A GRID WITH THE VERTICAL AXIS SHOWING THE TILT ANGLE AND THE HORIZONTAL AXIS SHOWING THE ROTATION ANGLE. THE GRID PIXELS VISUALISE THE NORMED VALUE OF THE DETECTABILITY INDEX OF THE CORRESPONDING PROJECTION WITH LIGHT COLOURS REPRESENTING A HIGH DETECTABILITY INDEX. THE THIRD AND THE FOURTH ROW SHOW SECTIONS OF THE RESULTING RECONSTRUCTIONS. THE THIRD ROW, I.E. THE Y-Z-PLANE, REPRESENTING THE SECTION THAT SHOULD HAVE OPTIMISED IMAGE QUALITY DUE TO THE CHOICE OF THE TASK FUNCTION WHICH IS VISUALISED IN (G)

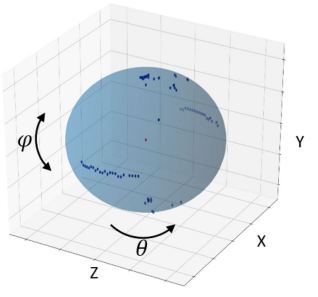
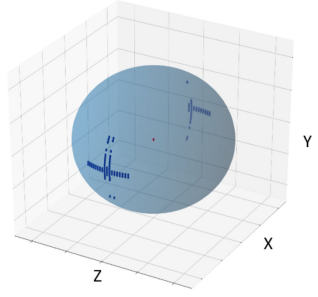
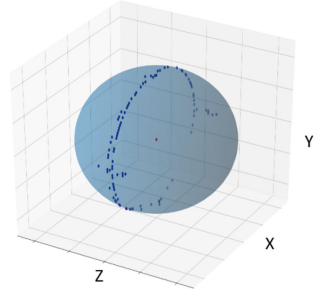
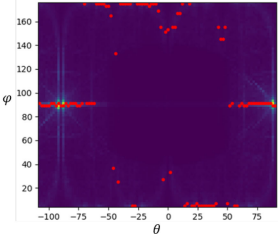
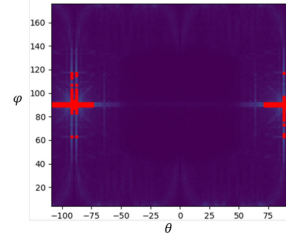
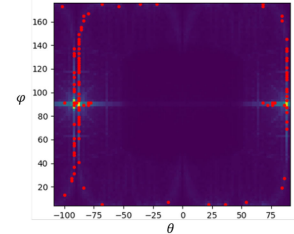
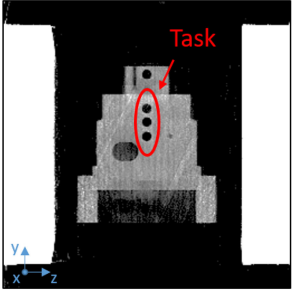
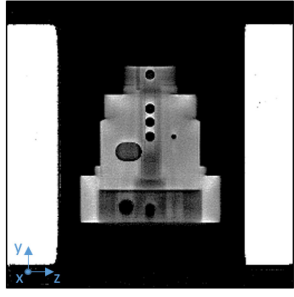
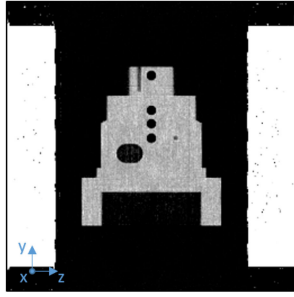
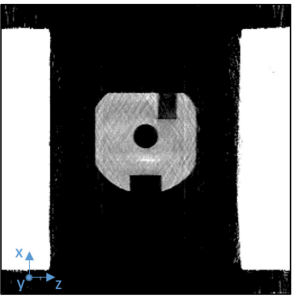
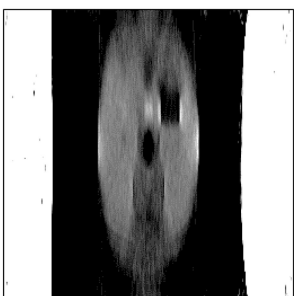
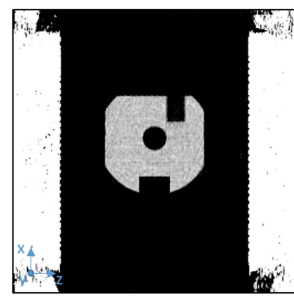
<i>OptDetectability</i>	<i>OptMax</i>	<i>OptCombined</i>
 <p>(a) 3D visualisation of the trajectory</p>	 <p>(b) 3D visualisation of the trajectory</p>	 <p>(c) 3D visualisation of the trajectory</p>
 <p>(d) Planar visualisation of the trajectory</p>	 <p>(e) Planar visualisation of the trajectory</p>	 <p>(f) Planar visualisation of the trajectory</p>
 <p>(g) Reconstruction, y-z-plane</p>	 <p>(h) Reconstruction, y-z-plane</p>	 <p>(i) Reconstruction, y-z-plane</p>
 <p>(j) Reconstruction, x-z-plane</p>	 <p>(k) Reconstruction, x-z-plane</p>	 <p>(l) Reconstruction, x-z-plane</p>

TABLE V

IMAGE METRICS OF EXPERIMENT 1B: EVALUATION OF THE PRESENTED MEASURE M_{Tuy} AS WELL AS THE CNR AND THE TV IMAGE METRIC ON SMALL, TASK-CENTRED REGIONS OF THE VOLUMES OF EXPERIMENT 1B

Method	CNR	TV	M_{Tuy}
$Opt_{Detectability}$	117.4	0.080	0.023
Opt_{Max}	34.2	0.068	0.088
$Opt_{Combined}$	291.1	0.072	0.002

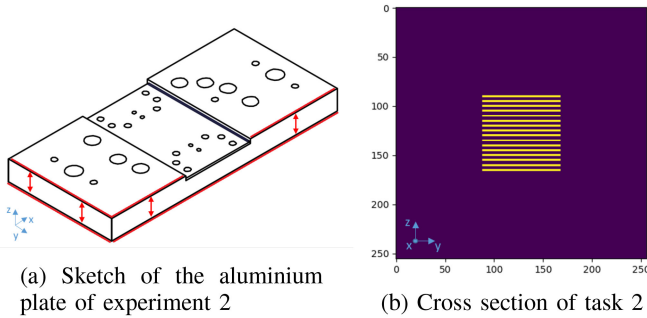


Fig. 8. Setting of experiment 2: Figure (a) shows a Sketch of the aluminium plate used in experiment 2 with red lines highlighting the edges of the top and bottom surfaces which are the task for the optimisation pROcess. Figure (b) shows a section of the task function in the y-z-plane consisting of parallel planes.

task as well as the overall image, depends strongly on the chosen basic trajectory. Opt_{Max} only focuses on the best views in relation to the detectability index and, hence, does not improve if there are more views with a relatively low detectability index. $Opt_{Combined}$ generates trajectories that optimise both, overall image quality and task-detectability. In experiment 1, it generated the comparatively best trajectories optimally utilising all available data.

B. Simulation Experiment 2

The goal of experiment 2 is to demonstrate how trajectories with a low number of projections can be found. The chosen task was to optimally visualise the top and bottom surfaces of an aluminium plate with several holes as shown in Fig. 8 a. Hence, planes parallel to these surfaces have been chosen as a suitable task function (see Fig. 8 b) in order to ensure that the detectability index increases if planar structures parallel to the y-z-plane are well detected.

With a geometrically simple object and an easy task, only a little number of projections is necessary to visualise the task. Hence, trajectories have been optimised with the goal of only $n := 10$ optimal projections.

In experiment 2, for Opt_{Max} and $Opt_{Combined}$ acquisition geometries on a sphere have been used as a basic trajectory with 100 rotational view angles equally distributed on an arc of 200° and possible tilt view angles between -85° and 85° angle from the horizontal in order to allow projections on a wide circular band (similar to experiment 1b). In $Opt_{Detectability}$ each rotation angle is assigned a tilt angle. Hence, in order to enable $Opt_{Detectability}$ to optimise the trajectory for only 10 projections, the number of rotation angles has to be decreased to 10. Both basic sets are visualised in Fig. 10.

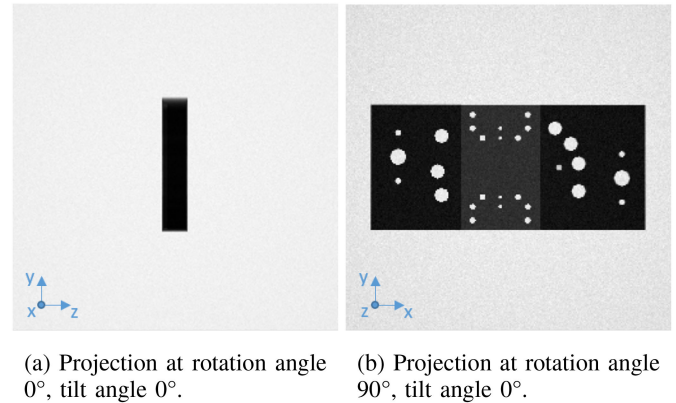


Fig. 9. Two Projections of the aluminium plate in experiment 2 scanned at different angles.

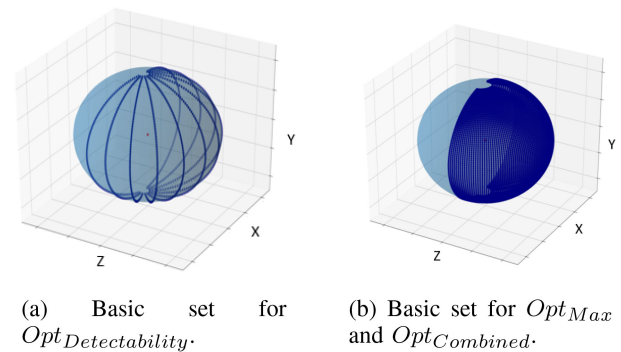


Fig. 10. Source positions of the basic trajectories of experiment 2. Every dark blue dot represents one source position.

The results of the optimisation pROcesses are visualised in Table VI.

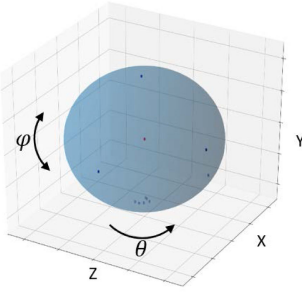
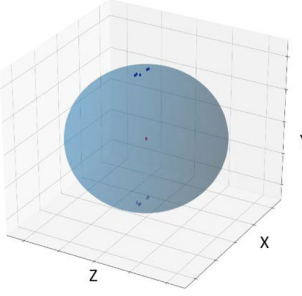
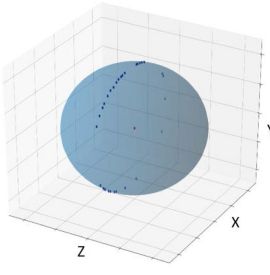
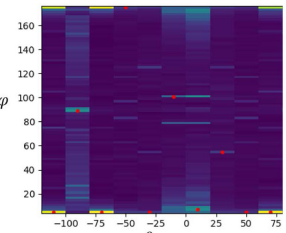
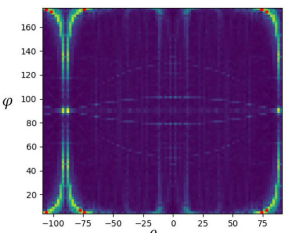
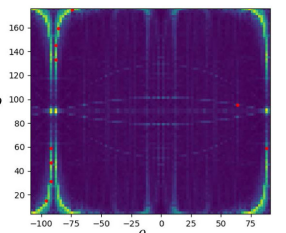
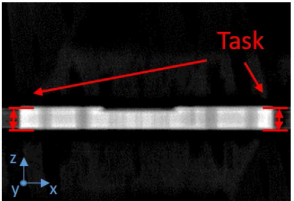
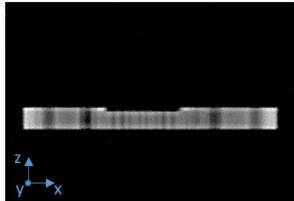
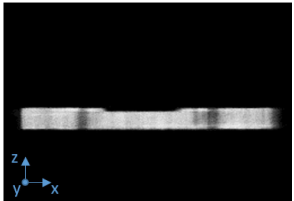
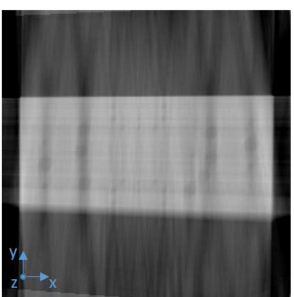
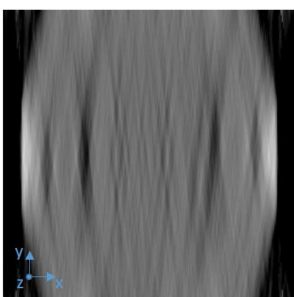
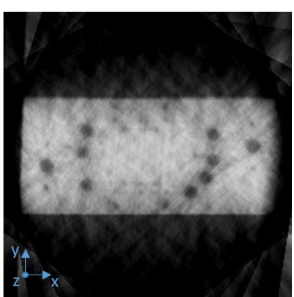
Despite only using 10 projections, all methods clearly visualise the task. Based on the visuals, the edges of the task are shaprest in Opt_{Max} and least sharp in $Opt_{Detectability}$. With only 10 projections, $Opt_{Combined}$ is the only method that leads to a roughly true overall representation of the structure of the object. Furthermore, to compare data completeness, the presented measure M_{Tuy} has been calculated. Opt_{Max} has the worst value of 0.149, $Opt_{Detectability}$ has a value of 0.046 and $Opt_{Combined}$ has the best value of 0.025. Again, this demonstrates that Opt_{Max} does not support data completeness, that $Opt_{Detectability}$ ensures some data completeness (based on the basic set) and that $Opt_{Combined}$ is able to ensure maximum data completeness.

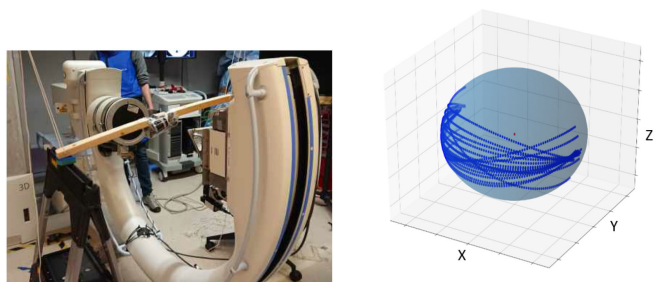
C. Measurement Data Experiment

In order to carry out experiments on trajectory optimisation with real data, but without the need of calibration of robots, the work of Thies *et al.* [20] was utilised. Thies *et al.* scanned a test specimen with a conventional CBCT scanner (Siemens Arcadis Orbic 3D). With this scanner, complex 3D trajectories can be generated, however, every tilt of the scanner would require calibration. Hence, instead of tilting the scanner to generate a 3D trajectory, the test specimen was placed in 17 different positions.

TABLE VI

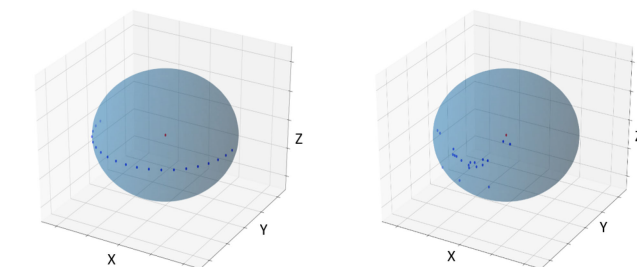
RESULTS OF EXPERIMENT 2: EACH COLUMN SHOWS THE RESULTS OF ONE OF THE OPTIMISATION ALGORITHMS. THE FIRST ROW SHOWS A 3D VISUALISATION OF THE TRAJECTORIES. EACH DARK BLUE DOT REPRESENTS THE SOURCE POSITION OF ONE ACQUISITION GEOMETRY. THE SECOND ROW SHOWS A PLANAR VISUALISATION OF THE TRAJECTORIES REPRESENTED BY RED DOTS ON A GRID WITH THE VERTICAL AXIS SHOWING THE TILT ANGLE AND THE HORIZONTAL AXIS SHOWING THE ROTATION ANGLE. THE GRID PIXELS VISUALISE THE NORMED VALUE OF THE DETECTABILITY INDEX OF THE CORRESPONDING PROJECTION WITH LIGHT COLOURS REPRESENTING A HIGH DETECTABILITY INDEX. THE THIRD AND THE FOURTH ROW SHOW SECTIONS OF THE RESULTING RECONSTRUCTIONS. THE THIRD ROW, I.E. THE X-Z-PLANE, REPRESENTING THE SECTION THAT SHOULD HAVE OPTIMISED IMAGE QUALITY DUE TO THE CHOICE OF THE TASK FUNCTION WHICH IS VISUALISED IN (G)

<i>Opt_{Detectability}</i> , 100 projections	<i>Opt_{Max}</i> , 30 projections	<i>Opt_{Combined}</i> , 30 projections
 <p>(a) 3D visualisation of the trajectory</p>	 <p>(b) 3D visualisation of the trajectory</p>	 <p>(c) 3D visualisation of the trajectory</p>
 <p>(d) Planar visualisation of the trajectory</p>	 <p>(e) Planar visualisation of the trajectory</p>	 <p>(f) Planar visualisation of the trajectory</p>
 <p>(g) Reconstruction with 100 projections, x-z-plane</p>	 <p>(h) Reconstruction with 30 projections, x-z-plane</p>	 <p>(i) Reconstruction with 30 projections, x-z-plane</p>
 <p>(j) Reconstruction with 100 projections, x-y-plane</p>	 <p>(k) Reconstruction with 30 projections, x-y-plane</p>	 <p>(l) Reconstruction with 30 projections, x-y-plane</p>



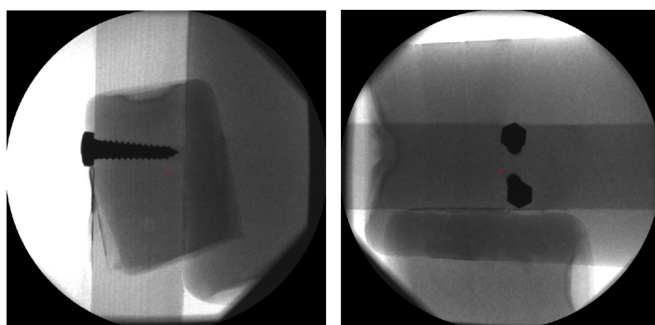
(a) Photograph of the C-arm CT with the probe for experiment 3. (b) Basic trajectory for experiment 3.

Fig. 11. Setting of experiment 3: Figure (a) is a photograph of the C-arm CT with the probe. Figure (b) visualises the source positions of the basic trajectory, a combination of different circular trajectories from Thies *et al.*



(a) A circular trajectory over 185°. (b) Trajectory of $Opt_{Combined}$.

Fig. 13. Trajectories for experiment 3: In (a) a single circle segment over an angular range of 185° with 20 projections is shown. In (b) the trajectory of $Opt_{Combined}$ with 20 projections is shown.



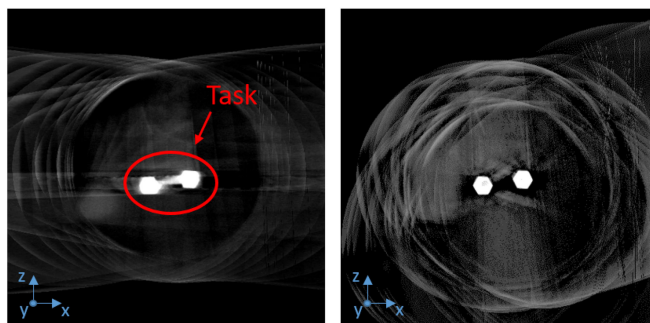
(a) Projection at rotation angle 0°. (b) Projection at rotation angle 90°.

Fig. 12. Projections of a test specimen consisting of two screws drilled into a wooden rod and two cylinders filled with ballistic gel for experiment 3.

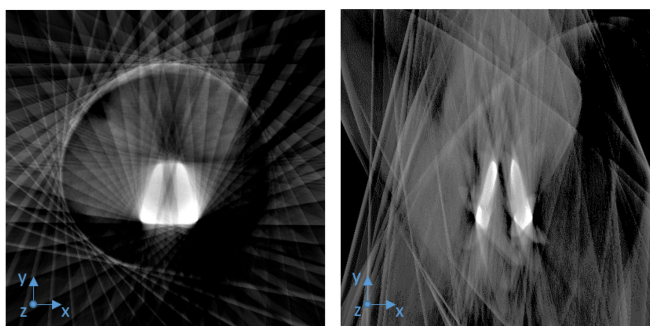
After reconstruction and registration of these 17 scans, the acquisition geometries of all scans were combined to one greater trajectory. At each position, 100 projections were generated over an angular range of 185°. The test specimen consists of two screws drilled into a wooden rod and two cylinders filled with ballistic gel. The setup as well as the resulting basic trajectory are visualised in Fig. 11. Two projections of the test specimen are shown in Fig. 12.

In this experiment, the goal is to optimally visualise the screw heads. As the screws are approximately cylindrical, a cylindrical task function was chosen like in experiment 1 visualised in Fig 4. Based on prior testing, the number of projections was set to 20. The optimisation was performed with $Opt_{Combined}$. The resulting trajectory of $Opt_{Combined}$ as well as a trajectory of a half circle for comparison are visualised in Fig. 13. The resulting reconstruction of $Opt_{Combined}$ as well as the reconstruction of the half circle are shown in Fig. 14.

The results clearly demonstrate that the task, the visualisation of the screw heads, was successfully optimised using $Opt_{Combined}$. With only 20 projections, the edges of the screw heads in the x-z-plane are sharp and show a high contrast to noise ratio. In contrast, the edges of the screw heads cannot be clearly seen in the reconstruction of the circular trajectory. Due to the focus on the task, other directions in the reconstruction



(a) Circular trajectory, x-z-plane. (b) $Opt_{Combined}$, x-z-plane.



(c) Circular trajectory, x-y-plane. (d) $Opt_{Combined}$, x-y-plane.

Fig. 14. Reconstruction results of experiment 3: (a) the x-z-plane of a circular trajectory, (b) x-z-plane of $Opt_{Combined}$, (c) x-y-plane of a circular trajectory and (d) x-y-plane of $Opt_{Combined}$. Figures (a) and (b) show the plane which contains the task.

of the trajectory of $Opt_{Combined}$, e.g. the x-y-plane, are of poor image quality with smears and blurred edges.

To summarise, experiment 3 demonstrates that the presented solution $Opt_{Combined}$ can be used to optimise trajectories for chosen tasks in real world applications. Furthermore, experiment 3 is an example for trajectory optimisation for the reduction of projections which could be utilised to reduce scan time and dose reduction.

IV. CONCLUSION

We have presented four solutions for trajectory optimisation, starting with preliminary work following Stayman *et al.*. We investigated differences as well as advantages and disadvantages of these methods and demonstrated them in several experiments.

In particular, we were able to show in experiment 1 that the developed methods are able to achieve high image quality even in the presence of metal parts. In experiments 2 and 3, we demonstrated that the presented methods can be used to find trajectories with few projections in order to reduce radiation dose and possibly the scan time. By optimising both, data quality and data completeness simultaneously with $Opt_{Combined}$, we are able to find arbitrary, task-driven trajectories without any artificial constraints. For the first time, this allows completely free, task-dependent trajectory optimisation without any additional user input.

In medicine, on the one hand, our solution can be used to find suitable trajectories for difficult scanning tasks with metal parts or limited space. On the other hand, our solution can be utilised to find trajectories with a reduced number of projections in order to decrease the radiation dose. In industry, together with the advent of twin-robotic CT systems, our solution enables scans with arbitrary geometries for scans of big objects, e.g. objects from the automotive or the aeronautics sector. For example, our method can be used to automatically find a trajectory for the example in the introduction, for scanning a rear light.

The optimisation solutions of this work have not yet been optimised for efficiency. Hence, the presented solutions have to be investigated and optimised further in order to enable practical, automatic trajectory computation. Furthermore, the following topics regarding the presented approaches need to be addressed in future work:

- This work presents a greedy optimisation approach. Due to the nature of greedy optimisation, the implemented greedy solver examines projections only in regard to the already chosen projections, but does not consider a complete trajectory. The implementation of a global optimiser would increase the results further by not only finding the next best projection, but the set of projections that complements each other best. Hence, a global solver could find a trajectory that leads to equal data completeness and quality with fewer projections or to increased data completeness and quality with the same amount of projections.
- In this work, the detectability index is developed for single projections separately. The joint evaluation of all chosen projections would probably improve the correlation to the resulting image quality.
- The presented approaches need simulations of all possible projections. This is costly and limits the optimisation to a finite, discrete set of projections. This should be addressed.
- In presented methods, the CT user has to define a basic set. Approaches for automatically determining a good basic set or approaches that do not need a basic set should be developed. This might need the incorporation of other sensory systems, e.g. RGB-D cameras as already presented in [21]–[23].

- In order to automatise the pROCESS further, a termination criterion should be added so that the number of projections does not have to be determined by the CT user.
- The results of the presented methods should be evaluated more thoroughly using task-focused image quality metrics.
- More comprehensive tests on real twin-robotic CT systems are imminent.

Finally, we want to emphasise that trajectory optimisation is only one of many fields of work to strengthen robotic CT systems in medicine and to establish them in industry. In order to enable accurate measurements with robotic CT systems, one of the big challenges is the calibration of the robots in order to compensate the robot's positioning errors. Another big challenge is the application of trajectory optimal 3D reconstruction methods, in particular for region of interest CT. Furthermore, previous knowledge is important for trajectory optimisation and reconstruction. Therefore, automatic methods for gathering previous knowledge have to be implemented. Lastly, we think that the biggest challenge for the establishment of robotic CT system in industry as well as medicine is user-friendliness. The handling of robot CT systems must be simple and the set-up times should be short compared to the scanning time.

REFERENCES

- [1] G. D. Rubin, "Computed tomography: Revolutionizing the practice of medicine for 40 years," *Radiology*, vol. 273, no. 2 pp. S45–S74, 2014.
- [2] L. de Chiffre, S. Carmignato, J.-P. Kruth, R. Schmitt, and A. Weckenmann, "Industrial applications of computed tomography," *CIRP Ann.*, vol. 63, no. 2, pp. 655–677, 2014.
- [3] J.-N. Zaech *et al.*, "Learning to avoid poor images: Towards task-aware c-arm cone-beam CT trajectories," in *Proc. Int. Conf. Med. Image Comput. Comput.-Assist. Intervention*, Cham, Germany, 2019, pp. 11–19.
- [4] G. Herl, J. Hiller, and T. Sauer, "Artifact reduction in x-ray computed tomography by multipositional data fusion using local image quality measures," in *Proc. 9th Conf. Ind. Computed Tomogr.*, 2019, pp. 13–15.
- [5] G. Herl, J. Hiller, and A. Maier, "Scanning trajectory optimisation using a quantitative tuiybased local quality estimation for robot-based x-ray computed tomography," *Nondestruct. Testing Eval.*, vol. 35, no. 3, pp. 287–303, 2020.
- [6] S. Akpek, T. Brunner, G. Benndorf, and C. Strother, "Three-dimensional imaging and cone beam volume CT in c-arm angiography with flat panel detector," *Diagn. Interventional Radiol.*, vol. 11, no. 1, pp. 10–13, 2005.
- [7] R. C. Orth, M. J. Wallace, and M. D. Kuo, "C-arm cone-beam CT: General principles and technical considerations for use in interventional radiology," *J. Vasc. Interventional Radiol.*, vol. 19, no. 6, pp. 814–820, 2008.
- [8] C. Czerny *et al.*, "Combining c-arm CT with a new remote operated positioning and guidance system for guidance of minimally invasive spine interventions," *J. NeuroInterventional Surg.*, vol. 7, no. 4, pp. 303–308, 2015.
- [9] S. Healthineers, "Multitom rax." Accessed: Mar. 3, 2021. [Online]. Available: <https://www.siemens-healthineers.com/no/robotic-x-ray/twin-robotic-x-ray/multitom-rax>
- [10] J. Hiller, P. Landstorfer, P. Marx, and M. Herbst, "Evaluation of the impact of faulty scanning trajectories in robot-based x-ray computed tomography," *Meas. Sci. Technol.*, vol. 32, no. 1, 2020, Art. no. 015401.
- [11] J. W. Stayman, S. Capostagno, G. J. Gang, and J. H. Siewerdsen, "Task-driven source-detector trajectories in cone-beam computed tomography: I theory and methods," *J. Med. Imag.*, vol. 6, no. 2, 2019, Art. no. 025002.
- [12] S. Hatamikia *et al.*, "Optimization for customized trajectories in cone beam computed tomography," *Med. Phys.*, vol. 47, no. 10, pp. 4786–4799, 2020.
- [13] Z. Zheng and K. Mueller, "Identifying sets of favorable projections for few-view low-dose cone-beam CT scanning," in *Proc. 11th Int. Meeting Fully Three-Dimensional Image Reconstruction Radiol. Nucl. Med.*, 2011, pp. 314–317.
- [14] A. Fischer, T. Lasser, M. Schrapp, J. Stephan, and P. B. Noël, "Object specific trajectory optimization for industrial x-ray computed tomography," *Sci. Rep.*, vol. 6, 2016, Art. no. 19135.

- [15] P. Wu *et al.*, “C-arm orbits for metal artifact avoidance (maa) in cone-beam CT,” *Phys. Med. Biol.*, vol. 65, no. 16, 2020, Art. no. 165012.
- [16] N. Hansen and S. Kern, “Evaluating the cma evolution strategy on multimodal test functions,” in *Proc. Int. Conf. Parallel Problem Solving Nat.*, Berlin, Heidelberg, Germany, 2004, pp. 282–291.
- [17] J. W. Stayman and J. H. Siewerdsen, “Task-based trajectories in iteratively reconstructed interventional cone-beam CT,” *Proc. 12th Int. Meeting Fully Three-Dimensional Image Reconst. Radiol. Nucl. Med.*, 2013, pp. 257–260.
- [18] H. K. Tuy, “An inversion formula for cone-beam reconstruction,” *SIAM J. Appl. Math.*, vol. 43, no. 3, pp. 546–552, 1983.
- [19] G. J. Gang, H. J. Siewerdsen, and J. W. Stayman, “Non-circular CT orbit design for elimination of metal artifacts,” *Med. Imag. 2020: Phys. Med. Imag.*, vol. 11312, 2020, Art. no. 1131227.
- [20] M. Thies *et al.*, “A learning-based method for online adjustment of c-arm cone-beam CT source trajectories for artifact avoidance,” *Int. J. Comput. Assist. Radiol. Surg.*, vol. 15, no. 11, pp. 1787–1796, 2020.
- [21] E. Tucker *et al.*, “Towards clinical translation of augmented orthopedic surgery: From pre-op CT to intra-op x-ray via RGBD sensing,” in *Med. Imag. 2018: Imag. Inform. Healthcare, Res. Appl.*, vol. 10579, 2018, Art. no. 105790J.
- [22] B. Bier *et al.*, “Motion compensation using range imaging in C-arm cone-beam CT,” in *Proc. Annu. Conf. Med. Image Understanding Anal.*, 2017, pp. 561–570.
- [23] B. Bier *et al.*, “Range imaging for motion compensation in C-arm cone-beam CT of knees under weight-bearing conditions,” *J. Imag.*, vol. 4, no. 1, pp. 561–570, 2018.



Gabriel Herl received the master’s degree in technomathematics from the Friedrich-Alexander University of Erlangen-Nuremberg, Germany, in 2015. Since then, he has been with the Deggendorf University of Technology, Germany, in close cooperation with the Fraunhofer Application Centre CTMT, as a Research Assistant with a focus on artefact reduction for CT applications and robotic CT systems.



Jochen Hiller has been Professor of X-ray computed tomography and measurement technology with the Faculty of Mechanical Engineering and Mechatronics, Deggendorf Institute of Technology, Germany, since 2014. His research interests include accuracy improvement of CT measurements, image artefact reduction methods, and robot-based CT.



Mareike Thies received the master’s degree in medical engineering from Friedrich-Alexander-University Erlangen-Nuremberg, Germany. In 2020, he joined the Pattern Recognition Lab, as Ph.D. candidate working on medical image reconstruction.



Jan-Nico Zaech is currently working toward the Ph.D. degree with Computer Vision Lab, ETH Zürich, Switzerland. In 2018, he graduated from Friedrich-Alexander-University Erlangen-Nuremberg, Germany. His research interests include computer vision and machine learning for autonomous systems.



Mathias Unberath is currently an Assistant Professor with the Department of Computer Science, Johns Hopkins University, Baltimore, MD, USA, with affiliations to the Laboratory for Computational Sensing and Robotics and the Malone Center for Engineering in Healthcare. He has created and is leading the Advanced Robotics and Computationally Augmented Environments (ARCADE) Lab that conducts research at the intersection of computer vision, machine learning, augmented reality, robotics, and imaging to develop collaborative intelligent systems.



Andreas Maier (Senior Member, IEEE) has been a Professor and the Head of the Department of Pattern Recognition, Friedrich-Alexander-University of Erlangen-Nuremberg, Germany, since 2015. His current research interests include medical imaging, image and audio processing, digital humanities, and interpretable machine learning and also the use of known operators.